A Novel Approach to Autonomous Lunar Localization and Timing

Fabio D'Onofrio* and Renato Zanetti†
The University of Texas at Austin, Austin, Texas, 78712

The ability of a deep-space spacecraft to estimate its position, velocity, and clock errors without external clock error estimation is investigated. A novel approach to onboard estimation of clock errors is proposed. The effects of clock bias and drift on spacecraft position and velocity errors are derived. These derived equations are leveraged to design a Kalman filter that processes optical measurements along with one-way ranging or two-way position updates from the ground. Simulations are performed to numerically validate the proposed approach and show good localization and timing estimation performance even with lengthy tracking data gaps.

Nomenclature

α,β	=	Crater centroid bearing angles with respect to the camera
b	=	True clock bias
$\hat{b}$	=	Estimated clock bias
d	=	True clock drift
f	=	Camera focal length
$\hat{d}$	=	Estimated clock drift
h_0,h_{-1},h_{-2}	=	Clock stability parameters
N	=	Image pixel length
$\boldsymbol{Q}_{acc}$	=	Acceleration process noise covariance matrix
$\boldsymbol{Q}_{clock}$	=	Clock process noise covariance matrix
$\boldsymbol{Q}_{posvel_k}$	=	Position-velocity process noise covariance matrix
$\boldsymbol{r}$	=	Spacecraft's position vector
$\boldsymbol{v}$	=	Spacecraft's velocity vector
$\boldsymbol{v}_{clock}$	=	Clock process noise
$\boldsymbol{v}_k$	=	Position-velocity process noise

*Graduate Research Assistant, Aerospace Engineering and Engineering Mechanics.
†Assistant Professor, Aerospace Engineering and Engineering Mechanics, AIAA Associate Fellow.

t	=	True time
$\hat{t}$	=	Estimated time
t_{clock}	=	Onboard time
x_c,y_c	=	Crater centroid pixel coordinates
x_p,y_p	=	Camera's principal point pixel coordinates

I. Introduction

Deep space position, navigation, and timing (PNT) is dominated by ground tracking via the Deep Space Network (DSN). Space vehicles typically establish a two-way communication connection with DSN, which allows the ground to form a precise position estimate (using so-called two-way ranging and doppler measurements) as well as estimate the onboard clock bias and drift. Ground-based orbit determination and onboard clock errors estimation avoids spacecraft timing errors to affect the navigation accuracy. While two-way communications is a common and precise way to relate the position and time of the spacecraft to the known position and time of the ground station(s), it also consumes ground resources and hence it is not an approach scalable to a very large number of spacecraft. Terrestrial and low-Earth orbit applications, on the other hand, typically rely on one-way ranging and doppler by processing signals from GNSS constellations. One-way ranging is possible because the large number of GNSS satellites generate many measurements with diverse geometry allowing for the estimation of both the receiver's position and its clock errors. Deep space one-way ranging from DSN stations does not provide sufficient measurement diversity to solve for both the orbit and onboard clock errors.

Much current work focuses on onboard deep space navigation without ground support [1, 2]. Proposed techniques include optical navigation with respect to distant planets/moons/asteroids/artificial satellites ([3–5]), with respect to lunar craters ([6–9]), or using the apparent size and position of the Earth and Moon disks ([10–12]). Other recent approaches include interlink ranging between various satellites in a non-Keplerian orbit (typically via third body perturbations), the so-called LiASON approach [13, 14] currently being tested in the Capstone mission [15]. Pulsar navigation is also a possible onboard deep space navigation approach, and encouraging preliminary results were obtained in a recent International Space Station experiment [16, 17]. Another approach to onboard deep space navigation relies on one-way ranging from ground stations, this approach is made possible by the Deep Space Atomic Clock, which allows for an extremely accurate estimate of the onboard time and is therefore able to form one-way ranging measurements [18–21].

The ability to precisely keep track of time onboard is crucial to performing accurate navigation, especially when a high level of autonomy is required. The Deep Space Atomic Clock is not an economically viable solution for many spacecraft, especially small ones, thus requiring the onboard time to be corrected to maintain the desired accuracy throughout the mission.

Different models for satellite clock offset exist, the most commonly accepted being a two– or three–states linear model [22, 23]. The first state is the clock bias, or offset, also referred to as the time interval error (TIE) [24], and represents the difference between the onboard time and the true time. The clock bias evolves as the integral of the clock drift, also called fractional frequency offset (because it is physically caused by the clock oscillator frequency error). It is also possible to include a third state to model the clock drift rate (also known as aging).

Once the clock offset model has been specified, its coefficients can be estimated through measurements relating the onboard time to a reference "true" time, for example using a least squares (LS) estimation process. Alternatively, a Kalman filter approach can be used. Reference 25 proposes a Kalman filter to estimate the clock states of an ensemble of clocks from observations of time differences between them. Reference 26 adds the capability to accept both time and frequency measurements, outliers rejection, and the ability to include any combination of white noises or random walk noises in all three clock states.

Clock estimation with a Kalman filter requires modeling of the process noise which must be deduced from the physical properties of the clock oscillator noise [27, 28]. Initial state estimate and estimation error covariance must also be specified. References 29 and 30 propose to relax these requirements by employing a finite impulse response unbiased estimation algorithm with measurements of the time interval error. They also compare the performance with a classic two-states clock Kalman filter with data from a real clock.

An adaptive Kalman filter with classified adaptive factors for clock offset estimation has also been proposed [31]. A long short-term memory (LSTM) machine learning approach to accurately express the nonlinear characteristics of the navigation satellite clock bias has been developed as well [32].

The aforementioned works estimate clock errors from time or frequency measurements of reference oscillators on the ground or on another satellite. They do not include a direct correlation between the clock offset and the position/velocity onboard propagation error. The aim of this work is to perform deep space onboard PNT without requiring heavy, power consuming, and/or expensive clocks (such as any ground-quality atomic clock) onboard our vehicle nor onboard other satellites our vehicle communicates with. This aim is achieved by two novel contributions of this work. First, we derive how onboard clock errors correlate to onboard position and velocity propagation errors. Using this model, we build correlations between localization errors and timing errors. Optical measurements generated onboard and referenced to the spacecraft time are used as navigation aids but they are unable to estimate the onboard time bias, for which periodic external measurements not affected by clock errors must be provided from ground. This leads to the second contribution of this work: relating one-way ranging signals to the spacecraft position and time, and using this information to update the onboard clock bias estimate.

The built-in correlation between timing and localization errors allows for the estimation of the onboard clock bias from range/position measurements time-tagged by an external source's accurate clock (as opposed to onboard generated measurements that are typically referenced to onboard time). As a use case, we examine the situation when two-way

communication with DSN can be established (for example in conjunction with telemetry downloads) and DSN uploads a position estimate of the spacecraft accompanied with a precise time-of-validity but without uplinking an estimate of the onboard clock bias correction.

We mechanize our approach with an extended Kalman filter; the filter state includes orbital position, velocity, clock bias and clock drift. The scenario in which simulations are carried out is the same as in Reference 9, in which a least squares solution is used to estimate a constant clock offset (that is, clock drift is assumed to be zero). We improve on the results of Reference 9 by accounting for clock drift and clock noise.

A similar problem and approach to this work was identified and investigated in Reference [33], although the authors do not include any direct correlation between the orbit states errors and the clock errors in the dynamics/error propagation.

The paper is organized as follows. First, the clock model and the filter covariance propagation equations are presented in detail in Section II. Section III describes the measurements and the update equations. Position, velocity and timing estimation performance is evaluated through numerical simulations shown in Section IV. Finally, conclusions are drawn in Section V.

II. Clock Model and Time Propagation

A. Clock model

The clock model adopted here is a two states linear model, which includes the clock bias, $b(t) = t_{clock} - t$ (where t_{clock} is the uncompensated onboard time and t is the true time), and a clock drift $d(t)$.

The filter equations are implemented in discrete time; we define the true time at the k-th step as t_k, the estimated time as $\hat{t}_k = \hat{t}(t_k)$, and the estimated time bias and drift as $\hat{b}_k = \hat{b}(t_k)$ and $\hat{d}_k = \hat{d}(t_k)$, respectively.

The clock true and estimated state dynamics equations in discrete time are:

$$\begin{bmatrix} b_{k+1} \\ d_{k+1} \end{bmatrix} = \begin{bmatrix} 1 & \Delta t_k \\ 0 & 1 \end{bmatrix} \begin{bmatrix} b_k \\ d_k \end{bmatrix} + \boldsymbol{\nu}_{clock}(t_k) \tag{1}$$

$$\begin{bmatrix} \hat{b}_{k+1} \\ \hat{d}_{k+1} \end{bmatrix} = \begin{bmatrix} 1 & \Delta \hat{t}_k \\ 0 & 1 \end{bmatrix} \begin{bmatrix} \hat{b}_k \\ \hat{d}_k \end{bmatrix} \tag{2}$$

where $\Delta \hat{t}_k = \hat{t}_{k+1} - \hat{t}_k$ is the estimated elapsed time between the two subsequent time steps and $\boldsymbol{\nu}_{clock}(t_k) \sim \mathcal{N}(\mathbf{0}, \boldsymbol{Q}_{clock}(t_k))$, that is, it is a two-dimensional Gaussian noise with zero mean and covariance matrix $\boldsymbol{Q}_{clock}(t_k)$

defined as in [27, 28]:

$$\boldsymbol{Q}_{clock} = \begin{bmatrix} q_{11} & q_{12} \\ q_{21} & q_{22} \end{bmatrix} \tag{3}$$

$$q_{11} = \frac{h_0}{2}\Delta\hat{t}_k + 2h_{-1}(\Delta\hat{t}_k)^2 + \frac{2}{3}\pi^2 h_{-2}(\Delta\hat{t}_k)^3 \tag{4}$$

$$q_{12} = q_{21} = h_{-1}\Delta\hat{t}_k + \pi^2 h_{-2}(\Delta\hat{t}_k)^2 \tag{5}$$

$$q_{22} = \frac{h_0}{2\Delta\hat{t}_k} + 4h_{-1} + \frac{8}{3}\pi^2 h_{-2}\Delta\hat{t}_k \tag{6}$$

The clock Allan parameters are chosen as $h_0 = 2e-19$s, $h_{-1} = 7e-21$ and $h_{-2} = 2e-20\text{s}^{-1}$. These values are taken from [28] and reflect the performance of of an inexpensive crystal oscillator. More details on this oscillator error model, including its Allan variance plot, can be also found in Reference [28].

The quantity $\Delta\hat{t}_k$ can be related to the estimate of the time drift as follows:

$$\begin{aligned} \Delta\hat{t}_k &= \hat{t}_{k+1} - \hat{t}_k = t_{clock}(t_{k+1}) - \hat{b}_{k+1} - \left(t_{clock}(t_k) - \hat{b}_k\right) \\ &= t_{clock}(t_{k+1}) - t_{clock}(t_k) - \hat{d}_k\ \Delta\hat{t}_k \end{aligned} \tag{7}$$

After some re-arranging:

$$\Delta\hat{t}_k = \left(t_{clock}(t_{k+1}) - t_{clock}(t_k)\right)/(1+\hat{d}_k) \tag{8}$$

This expression will be used in the next section to derive the state covariance propagation equations.

B. State and Covariance Propagation

Let $\boldsymbol{x}(t)$ be the state of a stochastic dynamic system (not including the clock bias and drift). The dynamics equations in continuous and discrete form can be written as:

$$\dot{\boldsymbol{x}}(t) = \boldsymbol{f}(\boldsymbol{x}(t), t) + \boldsymbol{\nu}(t) \tag{9}$$

$$\boldsymbol{x}_{k+1} = \boldsymbol{x}(t_{k+1}) = \boldsymbol{x}(t_k) + \int_{t_k}^{t_{k+1}} \boldsymbol{f}(\boldsymbol{x}(t), t)\ dt + \boldsymbol{\nu}_k \tag{10}$$

In our case, $\boldsymbol{x}(t) = \left[\boldsymbol{r}(t)^T, \boldsymbol{v}(t)^T\right]^T \in \mathcal{R}^6$ and the derivative function is $\boldsymbol{f}(\boldsymbol{x}(t), t) = [\boldsymbol{v}(t), \boldsymbol{a}(t)]$, where $\boldsymbol{a}(t)$ contains all gravitational and non-gravitational accelerations acting on the spacecraft. The process noise $\boldsymbol{\nu}_k$ is Gaussian

with zero mean and covariance $\boldsymbol{Q}_{posvel_k}$, which is generated using the linear process noise model [34], as:

$$\mathbf{Q}_{posvel_k} = \begin{bmatrix} \frac{1}{4}(\Delta\hat{t}_k)^4\, \boldsymbol{Q}_{acc} & \frac{1}{2}(\Delta\hat{t}_k)^3\, \boldsymbol{Q}_{acc} \\ \frac{1}{2}(\Delta\hat{t}_k)^3\, \boldsymbol{Q}_{acc} & (\Delta\hat{t}_k)^2\, \boldsymbol{Q}_{acc} \end{bmatrix}, \tag{11}$$

where $\boldsymbol{Q}_{acc}$ represents the process noise acceleration in inertial frame coordinates and is assumed diagonal:

$$\boldsymbol{Q}_{acc} = \begin{bmatrix} q_1 & 0 & 0 \\ 0 & q_2 & 0 \\ 0 & 0 & q_3 \end{bmatrix}$$

The estimated state at time t_k, $\hat{\boldsymbol{x}}_k = \hat{\boldsymbol{x}}(t_k)$, is propagated forward to t_{k+1} with our estimate of the time step $\Delta\hat{t}_k$:

$$\hat{\boldsymbol{x}}_{k+1} = \hat{\boldsymbol{x}}(t_{k+1}) = \hat{\boldsymbol{x}}_k + \int_0^{\Delta\hat{t}_k} \boldsymbol{f}(\hat{\boldsymbol{x}}(t_k+\tau), \hat{t}_k+\tau)\, d\tau \tag{12}$$

where $\Delta\hat{t}_k$ has been derived in Eq. (8).

The state estimation error is defined as:

$$\delta\boldsymbol{x}_{k+1} = \boldsymbol{x}_{k+1} - \hat{\boldsymbol{x}}_{k+1} = \boldsymbol{x}(t_{k+1}) - \hat{\boldsymbol{x}}(t_{k+1}) \tag{13}$$

The clock bias and drift estimation errors are similarly defined:

$$\begin{bmatrix} \delta b_k \\ \delta d_k \end{bmatrix} = \begin{bmatrix} b_k \\ d_k \end{bmatrix} - \begin{bmatrix} \hat{b}_k \\ \hat{d}_k \end{bmatrix} = \begin{bmatrix} b(t_k) \\ d(t_k) \end{bmatrix} - \begin{bmatrix} \hat{b}(t_k) \\ \hat{d}(t_k) \end{bmatrix} \tag{14}$$

Substituting Eq. (10) and Eq. (12) in Eq. (13), we have:

$$\begin{aligned} \delta\boldsymbol{x}_{k+1} &= \int_0^{\Delta t_k} \boldsymbol{f}(\boldsymbol{x}(t_k+\tau), t_k+\tau)\, d\tau + \boldsymbol{\nu}_k - \int_0^{\Delta\hat{t}_k} \boldsymbol{f}(\hat{\boldsymbol{x}}(t_k+\tau), \hat{t}_k+\tau)\, d\tau \\ &= \int_0^{\Delta t_k} \Big(\boldsymbol{f}(\boldsymbol{x}(t_k+\tau), t_k+\tau) - \boldsymbol{f}(\hat{\boldsymbol{x}}(t_k+\tau), \hat{t}_k+\tau)\Big)\, d\tau + \boldsymbol{\nu}_k - \int_{\Delta t_k}^{\Delta\hat{t}_k} \boldsymbol{f}(\hat{\boldsymbol{x}}(t_k+\tau), \hat{t}_k+\tau)\, d\tau \\ &= \int_0^{\Delta t_k} \Big(\boldsymbol{f}(\boldsymbol{x}(t_k+\tau), t_k+\tau) - \boldsymbol{f}(\hat{\boldsymbol{x}}(t_k+\tau), \hat{t}_k+\tau)\Big)\, d\tau + \boldsymbol{\nu}_k + \int_{\Delta\hat{t}_k}^{\Delta t_k} \boldsymbol{f}(\hat{\boldsymbol{x}}(t_k+\tau), \hat{t}_k+\tau)\, d\tau \\ &\approx \boldsymbol{F}(t_{k+1}, t_k)\, \delta\boldsymbol{x}_k - \left.\frac{\partial \boldsymbol{f}(\hat{\boldsymbol{x}}_k, t)}{\partial t}\right|_{\hat{t}_k} (t_k - \hat{t}_k)\, \Delta\hat{t}_k + \boldsymbol{\nu}_k + \boldsymbol{f}(\hat{\boldsymbol{x}}_{k+1}, \hat{t}_k + \Delta\hat{t}_k)\, \left(\Delta t_k - \Delta\hat{t}_k\right) \end{aligned} \tag{15}$$

where $\boldsymbol{F}(t_{k+1}, t_k)$ is the position-velocity state transition matrix from t_k to t_{k+1} and second and higher orders terms are

neglected. The term $(t_k - \hat{t}_k)$ (i.e. the error on estimated time) in Eq. (15) is equal to the error on the clock offset estimate, that is, $(t_k - \hat{t}_k) = \delta b_k$.

The true time step Δt_k can be expressed as a function of the drift estimation error δd_k, by starting from Eq. (8) and using Eq. (2), as follows:

$$\begin{aligned}\Delta\hat{t}_k &= \big(t_{clock}(t_{k+1}) - t_{clock}(t_k)\big)/\big(1+\hat{d}_k\big) = \big(t_{k+1} + b_{k+1} - t_k - b_k\big)/\big(1+\hat{d}_k\big) \\ &= \big(\Delta t_k + d_k \Delta t_k\big)/\big(1+\hat{d}_k\big) = \Delta t_k\big(1+d_k\big)/(1+\hat{d}_k\big)\end{aligned} \tag{16}$$

hence

$$\Delta t_k = \Delta\hat{t}_k \frac{1+\hat{d}_k}{1+d_k} \approx \Delta\hat{t}_k - \frac{\Delta\hat{t}_k}{1+\hat{d}_k}\,\delta d_k \tag{17}$$

The term $\big(\Delta t_k - \Delta\hat{t}_k\big)$ in Eq. (15) can then be written as $\big(-\frac{\Delta\hat{t}_k}{1+\hat{d}_k}\,\delta d_k\big)$.

Therefore, it is possible to write the position-velocity estimation error propagation equation as:

$$\delta\boldsymbol{x}_{k+1} = \boldsymbol{F}(t_{k+1}, t_k)\,\delta\boldsymbol{x}_k + \left[\left.\frac{\partial \boldsymbol{f}(\hat{\boldsymbol{x}}_k, t)}{\partial t}\right|_{\hat{t}_k} \Delta\hat{t}_k\right]\delta b_k + \left[-\boldsymbol{f}(\hat{\boldsymbol{x}}_{k+1}, \hat{t}_{k+1})\,\frac{\Delta\hat{t}_k}{1+\hat{d}_k}\right]\delta d_k + \boldsymbol{\nu}_k \tag{18}$$

The clock bias error is:

$$\begin{aligned}\delta b_{k+1} &= b_{k+1} - \hat{b}_{k+1} = b_k + d_k\Delta t_k + \boldsymbol{\nu}_{clock,b,k} - \hat{b}_k - \hat{d}_k\Delta\hat{t}_k \\ &\approx \delta b_k + (\delta d_k + \hat{d}_k)(\Delta\hat{t}_k - \frac{\Delta\hat{t}_k}{1+\hat{d}_k}\delta d_k) - \hat{d}_k\Delta\hat{t}_k + \boldsymbol{\nu}_{clock,b,k} \\ &\approx \delta b_k + \Delta\hat{t}_k\delta d_k - \frac{\Delta\hat{t}_k}{1+\hat{d}_k}\,\hat{d}_k\,\delta d_k + \boldsymbol{\nu}_{clock,b,k} \\ &= \delta b_k + \frac{\Delta\hat{t}_k}{1+\hat{d}_k}\,\delta d_k + \boldsymbol{\nu}_{clock,b,k}\end{aligned} \tag{19}$$

where, in the step from the second to the third line, the term $\hat{d}_k\Delta\hat{t}_k$ cancels out, and the second order term $\frac{\Delta\hat{t}_k}{1+\hat{d}_k}\delta d_k^2$ is neglected.

Finally, since the clock drift is assumed purely driven by noise, its estimation error propagates as:

$$\delta d_{k+1} = \delta d_k + \boldsymbol{\nu}_{clock,d,k} \tag{20}$$

The estimation error propagation equations are then written in matrix form as below:

$$\begin{bmatrix} \delta \boldsymbol{x}_{k+1} \\ \delta b_{k+1} \\ \delta d_{k+1} \end{bmatrix} = \begin{bmatrix} \boldsymbol{F}(t_{k+1}, t_k) & \left.\frac{\partial \boldsymbol{f}(\hat{\boldsymbol{x}}_k, t)}{\partial t}\right|_{\hat{t}_k} \Delta \hat{t}_k & -\boldsymbol{f}(\hat{\boldsymbol{x}}_{k+1}, \hat{t}_{k+1}) \frac{\Delta \hat{t}_k}{1+\hat{d}_k} \\ \boldsymbol{0} & 1 & \frac{\Delta \hat{t}_k}{1+\hat{d}_k} \\ \boldsymbol{0} & 0 & 1 \end{bmatrix} \begin{bmatrix} \delta \boldsymbol{x}_k \\ \delta b_k \\ \delta d_k \end{bmatrix} + \begin{bmatrix} \boldsymbol{\nu}_k \\ \boldsymbol{\nu}_{clock,b,k} \\ \boldsymbol{\nu}_{clock,d,k} \end{bmatrix} \tag{21}$$

The above equation is in the form:

$$\boldsymbol{e}_{k+1} = \boldsymbol{\Phi}_k \boldsymbol{e}_k + \overline{\boldsymbol{\nu}}_k \tag{22}$$

Therefore, the predicted estimation error covariance at time $(k+1)$, $\bar{P}_{k+1}$, is obtained as:

$$\bar{P}_{k+1} = \boldsymbol{\Phi}_k \boldsymbol{P}_k \boldsymbol{\Phi}_k^{\mathrm{T}} + \boldsymbol{Q}_k \tag{23}$$

Where $\boldsymbol{Q}_k = diag(\boldsymbol{Q}_{posvel_k}, \boldsymbol{Q}_{clock_k})$ is the full (eight by eight) state process noise covariance, which comprises the six by six position/velocity block $\boldsymbol{Q}_{posvel_k}$, defined in Eq. (11), and the two by two clock process noise block $\boldsymbol{Q}_{clock_k}$ defined in Eq. 3. It is assumed that the translational states noise is uncorrelated from the clock states noise.

III. Measurement update

Two types of external measurements are considered. The first one is a position measurement provided from ground, obtained by processing batches of DSN range and range rate measurements via two-way ranging; the second consists of DSN one-way ranging measurements.

A. Craters measurement update

The first type of measurement available to the spacecraft, time-tagged by the onboard clock, is given by bearing angles α and β that represent the location of crater centroids with respect to the camera.These angles are computed as:

$$\alpha = \arctan\left(\frac{x_c - x_p}{f}\right) \tag{24}$$

$$\beta = \arctan\left(\frac{y_c - x_p}{f}\right), \tag{25}$$

where x_c ,y_c are the crater centroid pixel coordinates, x_p ,y_p are the principal point pixel coordinates, and f is the camera focal length (expressed in units of pixels).

Every time a new image is acquired, a certain number of craters are detected through a Mask R-CNN detector, and are then matched to craters of an onboard catalog. The reader is referred to Reference 9 for further details about the

detection and matching algorithms.

In order to compute the expected measurement, which is needed to obtain the residual in the classic Kalman filter formulation, the bearing angles are calculated using the vector from the camera to the crater centroid at estimated time, $\boldsymbol{r}_{cr}^{CAM}(\hat{t}_k)$. This vector is first computed in the MCI frame, and then transformed in camera frame:

$$\hat{\boldsymbol{r}}_{cr}^{CAM}(\hat{t}_k) = \begin{bmatrix} \hat{x}_k \\ \hat{y}_k \\ \hat{z}_k \end{bmatrix} = \hat{\boldsymbol{T}}_{MCI}^{CAM}(\hat{t}_k)\left(\hat{\boldsymbol{T}}_{MCMF}^{MCI}(\hat{t}_k)\boldsymbol{r}_{cr}^{MCMF}(\hat{t}_k) - \hat{\boldsymbol{r}}_{MCI}(\hat{t}_k)\right) \tag{26}$$

$$\hat{\boldsymbol{T}}_{MCI}^{CAM}(\hat{t}_k) = \boldsymbol{T}_{B}^{CAM}\hat{\boldsymbol{T}}_{MCI}^{B}(\hat{t}_k) \tag{27}$$

where $\boldsymbol{r}_{cr}^{MCI}(\hat{t}_k)$ and $\hat{\boldsymbol{r}}^{MCI}(\hat{t}_k)$ are the crater centroid and spacecraft center of mass positions in the Moon Centered Inertial (MCI) frame at estimated time, respectively. $\hat{\boldsymbol{T}}_{MCI}^{CAM}(\hat{t}_k)$ is the direction cosine matrix to change coordinates from the MCI frame to the camera frame, $\hat{\boldsymbol{T}}_{MCMF}^{MCI}(\hat{t}_k)$ is the transformation matrix from the Moon Centered Moon Fixed (MCMF) frame to the MCI frame, and the subscript B represents the body frame. The spacecraft body frame is assumed aligned with the North-East-Down frame.

The expected measurement can then be computed as:

$$\hat{\boldsymbol{y}}_k = \hat{\boldsymbol{y}}(\hat{t}_k) = \begin{bmatrix} \hat{\alpha}_k \\ \hat{\beta}_k \end{bmatrix} + \boldsymbol{w}_k = \begin{bmatrix} \text{atan}(\hat{x}_k/\hat{z}_k) \\ \text{atan}(\hat{y}_k/\hat{z}_k) \end{bmatrix} + \boldsymbol{w}_k \tag{28}$$

where the measurement noise $\boldsymbol{w}_k$ is assumed gaussian with zero mean and covariance matrix $\boldsymbol{R}_k$.

The measurement partials are

$$\frac{\partial \boldsymbol{y}_k}{\partial \hat{\boldsymbol{r}}} = \frac{\partial \boldsymbol{y}_k}{\partial \hat{\boldsymbol{r}}_{cr}^{CAM}} \frac{\partial \hat{\boldsymbol{r}}_{cr}^{CAM}}{\partial \hat{\boldsymbol{r}}} \tag{29}$$

$$\frac{\partial \boldsymbol{y}_k}{\partial \hat{b}_k} = \begin{bmatrix} \frac{\partial \hat{\alpha}_k}{\partial \hat{b}_k} \\ \frac{\partial \hat{\beta}_k}{\partial \hat{b}_k} \end{bmatrix} = \frac{\partial \boldsymbol{y}_k}{\partial \hat{\boldsymbol{r}}_{cr}^{CAM}} \frac{\partial\, \hat{\boldsymbol{r}}_{cr}^{CAM}}{\partial \hat{b}_k} \tag{30}$$

with:

$$\frac{\partial \boldsymbol{y}_k}{\partial \hat{\boldsymbol{r}}_{cr}^{CAM}} = \begin{bmatrix} \hat{z}_k/(\hat{x}_k^2+\hat{z}_k^2) & 0 & -\hat{x}_k/(\hat{x}_k^2+\hat{z}_k^2) \\ 0 & \hat{z}_k/(\hat{y}_k^2+\hat{z}_k^2) & -\hat{y}_k/(\hat{y}_k^2+\hat{z}_k^2) \end{bmatrix} \tag{31}$$

$$\frac{\partial \hat{\boldsymbol{r}}_{cr}^{CAM}}{\partial \hat{\boldsymbol{r}}} = -\boldsymbol{T}_B^{CAM}\hat{\boldsymbol{T}}_{MCI}^{B}(\hat{t}_k) \tag{32}$$

$$\begin{aligned} \frac{\partial \boldsymbol{r}_{cr}^{CAM}}{\partial \hat{b}_k} &= \boldsymbol{T}_B^{CAM}\hat{\boldsymbol{T}}_{MCI}^{B}(\hat{t}_k)\frac{\partial \hat{\boldsymbol{T}}_{MCMF}^{MCI}(\hat{t}_k)}{\partial \hat{t}_k}\frac{\partial \delta t_k}{\partial \delta b_k}\left[\boldsymbol{r}_{cr}(\hat{t}_k)\right]_{MCMF} \\ &= \boldsymbol{T}_B^{CAM}\hat{\boldsymbol{T}}_{MCI}^{B}(\hat{t}_k)\frac{\partial \hat{\boldsymbol{T}}_{MCMF}^{MCI}(\hat{t}_k)}{\partial \hat{t}_k}\left[\boldsymbol{r}_{cr}(\hat{t}_k)\right]_{MCMF} \end{aligned} \tag{33}$$

The term $\frac{\partial \hat{\boldsymbol{T}}_{MCMF}^{MCI}(\hat{t}_k)}{\partial \hat{t}_k}$ is the derivative, with respect to the estimated time, of the MCMF to MCI rotation matrix, and $\frac{\partial \delta t_k}{\partial \delta b_k} = 1$, since $\delta t_k = \delta b_k$ as described previously. Essentially, the clock error affects the computation of this transformation matrix because of its dependence on the estimated time.

The partials with respect to the spacecraft velocity and the clock drift are zero. The measurement partial matrix $\boldsymbol{H}_k$ is then:

$$\boldsymbol{H}_k = \begin{bmatrix} \hat{z}_k/(\hat{x}_k^2+\hat{z}_k^2) & 0 & -\hat{x}_k/(\hat{x}_k^2+\hat{z}_k^2) & 0 & 0 & 0 & \frac{\partial \hat{\alpha}_k}{\partial \hat{b}_k} & 0 \\ 0 & \hat{z}_k/(\hat{y}_k^2+\hat{z}_k^2) & -\hat{y}_k/(\hat{y}_k^2+\hat{z}_k^2) & 0 & 0 & 0 & \frac{\partial \hat{\beta}_k}{\partial \hat{b}_k} & 0 \end{bmatrix} \tag{34}$$

where the expressions of $\frac{\partial \hat{\alpha}_k}{\partial \hat{b}_k}$ and $\frac{\partial \hat{\beta}_k}{\partial \hat{b}_k}$ were given in Eq. 30,32,33.

The Kalman gain and the updated full state are then computed as:

$$\mathbf{K}_k = \bar{\boldsymbol{P}}_k\mathbf{H}_k^T\left(\mathbf{H}_k\bar{\boldsymbol{P}}\mathbf{H}_k^T + \mathbf{R}_k\right)^{-1} \tag{35}$$

$$\hat{\boldsymbol{x}}_k = \bar{\boldsymbol{x}}_k + \boldsymbol{K}_k(\boldsymbol{y}_k - \hat{\boldsymbol{y}}_k) \tag{36}$$

where $\bar{\boldsymbol{x}}_k$ and $\bar{\boldsymbol{P}}$ are the predicted state and covariance at time k, obtained by propagating the estimated state and covariance from $\hat{t}_{k-1}$ to $\hat{t}_k$ through Eq. (21) and Eq. (23), respectively.

B. One-way ranging

When performing DSN one-way ranging, the ground station broadcasts a signal according to its precise and accurate ground clock while the spacecraft is subject to onboard clock errors. Hence the spacecraft receives a pseudorange measurement affected by the clock bias b. The range measurement ρ_k is modeled as follows:

$$\rho_k = \rho(\hat{t}_k) = (t_k + b_k - t_k^t)\,c = ||\boldsymbol{r}^{MCI}(t_k) - \boldsymbol{r}_{\boldsymbol{station}}^{MCI}(t_k^t)|| + c\,b_k \tag{37}$$

where c is the speed of light, t_k is the receive time, t_k^t is the transmit time, $\boldsymbol{r}_{\boldsymbol{station}}^{\boldsymbol{MCI}}(t_k^t)$ is the DSN station position in MCI at time of transmission, $\boldsymbol{r}^{\boldsymbol{MCI}}(t_k)$ is the spacecraft position vector in MCI at time of reception.

The time of transmission t_k^t is known very accurately (up to the accuracy of DSN's ground -kept time), while the time of reception is affected by onboard clock errors. The measurement residual is given by

$$\rho_k - \hat{\rho}_k = ||\boldsymbol{r}^{MCI}(t_k) - \boldsymbol{r}_{\boldsymbol{station}}^{MCI}(t_k^t)|| + c\ b_k - ||\hat{\boldsymbol{r}}^{MCI}(\hat{t}_k) - \boldsymbol{r}_{\boldsymbol{station}}^{MCI}(t_k^t)|| - c\ \hat{b}_k \tag{38}$$

$$\approx ||\boldsymbol{r}^{MCI}(\hat{t}_k) + \boldsymbol{v}^{MCI}(\hat{t}_k)\ (t_k - \hat{t}_k) - \boldsymbol{r}_{\boldsymbol{station}}^{MCI}(t_k^t)|| + c\ b_k - ||\hat{\boldsymbol{r}}^{MCI}(\hat{t}_k) - \boldsymbol{r}_{\boldsymbol{station}}^{MCI}(t_k^t)|| - c\ \hat{b}_k \tag{39}$$

$$= ||\boldsymbol{r}^{MCI}(\hat{t}_k) + \boldsymbol{v}^{MCI}(\hat{t}_k)\ \delta b_k - \boldsymbol{r}_{\boldsymbol{station}}^{MCI}(t_k^t)|| - ||\hat{\boldsymbol{r}}^{MCI}(\hat{t}_k) - \boldsymbol{r}_{\boldsymbol{station}}^{MCI}(t_k^t)|| + c\ \delta b_k \tag{40}$$

$$\approx \frac{[\hat{\boldsymbol{r}}^{MCI}(\hat{t}_k) - \boldsymbol{r}_{\boldsymbol{station}}^{MCI}(t_k^t)]^T}{||\hat{\boldsymbol{r}}^{MCI}(\hat{t}_k) - \boldsymbol{r}_{\boldsymbol{station}}^{MCI}(t_k^t)||}\delta\hat{\boldsymbol{r}}^{MCI}(\hat{t}_k) + \frac{[\hat{\boldsymbol{r}}^{MCI}(\hat{t}_k) - \boldsymbol{r}_{\boldsymbol{station}}^{MCI}(t_k^t)]^T}{||\hat{\boldsymbol{r}}^{MCI}(\hat{t}_k) - \boldsymbol{r}_{\boldsymbol{station}}^{MCI}(t_k^t)||}\hat{\boldsymbol{v}}^{MCI}(\hat{t}_k)\ \delta b_k + c\ \delta b_k \tag{41}$$

$$\approx \frac{[\hat{\boldsymbol{r}}^{MCI}(\hat{t}_k) - \boldsymbol{r}_{\boldsymbol{station}}^{MCI}(t_k^t)]^T}{||\hat{\boldsymbol{r}}^{MCI}(\hat{t}_k) - \boldsymbol{r}_{\boldsymbol{station}}^{MCI}(t_k^t)||}\delta\hat{\boldsymbol{r}}^{MCI}(\hat{t}_k) + c\ \delta b_k \tag{42}$$

the second term of equation (41) is negligible with respect to the third because the spacecraft's velocity is much smaller than the speed of light.

The Kalman gain and state update equations are:

$$\boldsymbol{K}_k = \bar{\boldsymbol{P}}_k \boldsymbol{H}_\rho^{\mathrm{T}}\left(\boldsymbol{H}_\rho \bar{\boldsymbol{P}}_k \boldsymbol{H}_\rho^{\mathrm{T}} + \boldsymbol{R}_k\right)^{-1} \tag{43}$$

$$\hat{\boldsymbol{x}}_k = \bar{\boldsymbol{x}}_k + \boldsymbol{K}_k(\rho_k - \hat{\rho}_k) \tag{44}$$

in which $\boldsymbol{H}_\rho \in \mathcal{R}^{1\times 8}$ is the matrix of partials of spacecraft-to-station range with respect to the filter state and it is given by

$$\boldsymbol{H}_\rho = \frac{\partial\rho_k}{\partial\boldsymbol{x}} = \frac{\partial\rho_k}{\partial\begin{bmatrix}\left(\boldsymbol{r}^{MCI}\right)^T & \left(\boldsymbol{v}^{MCI}\right)^T & b & d\end{bmatrix}^T} = \begin{bmatrix}\frac{[\boldsymbol{r}^{MCI}(\hat{t}_k) - \boldsymbol{r}_{\boldsymbol{station}}^{MCI}(t_k^t)]^T}{||\boldsymbol{r}^{MCI}(\hat{t}_k) - \boldsymbol{r}_{\boldsymbol{station}}^{MCI}(t_k^t)||} & \boldsymbol{O}_{1\times 3} & c & 0\end{bmatrix} \tag{45}$$

C. Ground position update

A possibility arising from explicitly accounting for the correlations between timing and localization errors is to estimate the clock errors from position measurements time tagged with true time rather than onboard time. This situation can occur, for example, when DSN tracks a satellite, performs orbit determination on it, and uploads the result which is then used by the satellite as an external measurement. Let $\boldsymbol{p}_j$ be the position measurement provided from the ground, time-tagged with the precisely kept ground time t_j.

The proposed approach starts by propagating the state and state transition matrix from the current estimated time $\hat{t}_k$ to time t_j. The equations used will be slightly different from the ones derived before, because t_j does not contain the

onboard clock offset. Let Δt_j and $\Delta \hat{t}_j$ be the true and estimated elapsed times from current time to the ground update time:

$$\Delta t_j = t_j - t_k \tag{46}$$

$$\Delta \hat{t}_j = t_j - \hat{t}_k = t_j - t_k - \delta b_k = \Delta t_j - \delta b_k \tag{47}$$

The difference $(\Delta t_j - \Delta \hat{t}_j)$ is then given by the error on estimated clock bias δb_k.

Position, velocity, and clock states are propagated as:

$$\hat{\boldsymbol{x}}_j = \hat{\boldsymbol{x}}_k + \int_0^{\Delta \hat{t}_j} \boldsymbol{f}(\hat{\boldsymbol{x}}(t_k + \tau), \hat{t}_k + \tau)\, d\tau \tag{48}$$

$$\begin{bmatrix} \hat{b}_j \\ \hat{d}_j \end{bmatrix} = \begin{bmatrix} 1 & \Delta \hat{t}_j \\ 0 & 1 \end{bmatrix} \begin{bmatrix} \hat{b}_k \\ \hat{d}_k \end{bmatrix} \tag{49}$$

To derive the state transition matrix from $\hat{t}_k$ to t_j, we start again from the state estimation error:

$$\begin{aligned}
\delta \boldsymbol{x}_j = \boldsymbol{x}_j - \hat{\boldsymbol{x}}_j &= \int_0^{\Delta t_j} \boldsymbol{f}(\boldsymbol{x}(t_k + \tau), t_k + \tau)\, d\tau + \boldsymbol{\nu}_k - \int_0^{\Delta \hat{t}_j} \boldsymbol{f}(\hat{\boldsymbol{x}}(t_k + \tau), \hat{t}_k + \tau)\, d\tau \\
&= \int_0^{\Delta t_j} \Big(\boldsymbol{f}(\boldsymbol{x}(t_k + \tau), t_k + \tau) - \boldsymbol{f}(\hat{\boldsymbol{x}}(t_k + \tau), \hat{t}_k + \tau) \Big)\, d\tau + \boldsymbol{\nu}_k - \int_{\Delta t_j}^{\Delta \hat{t}_j} \boldsymbol{f}(\hat{\boldsymbol{x}}(t_k + \tau), \hat{t}_k + \tau)\, d\tau \\
&\approx \boldsymbol{F}(t_j, t_k)\, \delta \boldsymbol{x}_k + \left. \frac{\partial \boldsymbol{f}(\hat{\boldsymbol{x}}_k, t)}{\partial t} \right|_{\hat{t}_k} \delta b_k\, \Delta \hat{t}_j + \boldsymbol{\nu}_k + \boldsymbol{f}(\hat{\boldsymbol{x}}_j, \hat{t}_j)\, \left(\Delta t_j - \Delta \hat{t}_j \right) \\
&= \boldsymbol{F}(t_j, t_k)\, \delta \boldsymbol{x}_k + \left[\left. \frac{\partial \boldsymbol{f}(\hat{\boldsymbol{x}}_k, t)}{\partial t} \right|_{\hat{t}_k} \Delta \hat{t}_j + \boldsymbol{f}(\hat{\boldsymbol{x}}_j, \hat{t}_j) \right] \delta b_k + \boldsymbol{\nu}_k
\end{aligned} \tag{50}$$

The clock bias estimation error evolves as:

$$\begin{aligned}
\delta b_j = b_j - \hat{b}_j &= b_k + d_k \Delta t_j - \hat{b}_k - \hat{d}_k \Delta \hat{t}_j \\
&= \delta b_k + (\hat{d}_k + \delta d_k)(\Delta \hat{t}_j + \delta b_k) - \hat{d}_k \Delta \hat{t}_j \\
&= \delta b_k + \hat{d}_k \Delta \hat{t}_j + \Delta \hat{t}_j \delta d_k + \hat{d}_k \delta b_k + \delta d_k \delta b_k - \hat{d}_k \Delta \hat{t}_j \\
&\approx \delta b_k + \hat{d}_k\, \delta b_k + \Delta \hat{t}_j \delta d_k = (1 + \hat{d}_k) \delta b_k + \Delta \hat{t}_j \delta d_k
\end{aligned} \tag{51}$$

where the second order term $\delta d_k \delta b_k$ is neglected. The drift estimation error evolves as:

$$\delta d_j = \delta d_k \tag{52}$$

The estimation error propagation equations can be written in matrix form as:

$$\begin{bmatrix} \delta \boldsymbol{x}_j \\ \delta b_j \\ \delta d_j \end{bmatrix} = \begin{bmatrix} \boldsymbol{F}(t_j, t_k) & \left.\frac{\partial \boldsymbol{f}(\hat{\boldsymbol{x}}_k, t)}{\partial t}\right|_{\hat{t}_k} \Delta \hat{t}_j + \boldsymbol{f}(\hat{\boldsymbol{x}}_j, \hat{t}_j) & \boldsymbol{0} \\ \boldsymbol{0} & 1 + \hat{d}_k & \Delta \hat{t}_j \\ \boldsymbol{0} & 0 & 1 \end{bmatrix} \begin{bmatrix} \delta \boldsymbol{x}_k \\ \delta b_k \\ \delta d_k \end{bmatrix} + \begin{bmatrix} \boldsymbol{\nu}_k \\ 0 \\ 0 \end{bmatrix} \tag{53}$$

which is in the form:

$$\boldsymbol{e}_j = \boldsymbol{\Phi}(t_j, t_k)\boldsymbol{e}_k + \overline{\boldsymbol{\nu}}_k \tag{54}$$

Therefore, when a ground measurement is received, Kalman gain computations and state update are performed as follows:

$$\boldsymbol{K}_k = \bar{\boldsymbol{P}}_k \big(\boldsymbol{H}_g \boldsymbol{\Phi}(t_j, t_k)\big)^{\mathrm{T}} \Big(\big(\boldsymbol{H}_g \boldsymbol{\Phi}(t_j, t_k)\big) \bar{\boldsymbol{P}}_k \big(\boldsymbol{H}_g \boldsymbol{\Phi}(t_j, t_k)\big)^{\mathrm{T}} + \boldsymbol{R}_{pos_j} \Big)^{-1} \tag{55}$$

$$\hat{\boldsymbol{x}}_k = \bar{\boldsymbol{x}}_k + \boldsymbol{K}_k (\boldsymbol{p}_j - \boldsymbol{H}_g \bar{\boldsymbol{x}}_j) \tag{56}$$

where $\boldsymbol{H}_g \in \mathcal{R}^{3\times 8}$ is the matrix of partials of ground measurement equation,

$$\boldsymbol{H}_g = \frac{\partial \boldsymbol{p}_j}{\partial \boldsymbol{x}} = \frac{\partial \boldsymbol{r}^{MCI}}{\partial \begin{bmatrix} \left(\boldsymbol{r}^{MCI}\right)^T & \left(\boldsymbol{v}^{MCI}\right)^T & b & d \end{bmatrix}^T} = \begin{bmatrix} \boldsymbol{I}_3 & \boldsymbol{O}_{3\times 5} \end{bmatrix} \tag{57}$$

and $\boldsymbol{R}_{pos_j}$ is the ground position measurement noise covariance matrix.

IV. Numerical Simulation

This section presents simulations of a spacecraft in a 100 km circular and equatorial orbit around the Moon. The onboard camera takes an image of the Moon surface every 5 seconds. The data sources to generate images in our simulations is the LROC Global Morphologic Maps [35] and the Robbins lunar crater database. [36] Each image is given as an input to a Mask R-CNN detector, and is assigned a confidence value to remove false detections (detected craters with a confidence value lower than the threshold are not passed to the filter). Each detected crater is fitted to an ellipse whose center gives the crater centroid pixel coordinates expressed in the camera frame, x_c and y_c. These coordinates are then used to match the detected craters to craters in the surface feature catalog available to the spacecraft (the Robbins lunar crater catalog). From this database, a local catalog is created at each time step by projecting the spacecraft camera's field of view pointing downward towards the surface according to the spacecraft's body frame (coinciding with the North-East-Down frame). After a local catalog is created, the Munkres or Hungarian Matching algorithm [37]·[38] is used to identify craters based on entries in the crater catalog. Camera images' timestamps are

perturbed with clock errors simulated through the model previously described .

Additional measurements are one or two way ranging from DSN stations. Spacecraft-to-station visibility is modeled by taking into account the relative position of Earth, Moon, and the spacecraft. No atmospheric delays are modeled in the DSN measurements. The spacecraft's attitude is assumed to be such that the camera is always pointing downward to the Moon surface.

The dynamics model includes a spherical harmonic model for the Moon gravity, plus Earth and Sun as third body perturbations. The filter propagates the dynamics in the Moon Centered Inertial (MCI) frame, the onboard state is 8-dimensional (shown in Table 1).

Table 1 Filter estimated states

State	# of Elements	Description
$\boldsymbol{r}^{MCI}$	3	Spacecraft position in MCI frame
$\boldsymbol{v}^{MCI}$	3	Spacecraft velocity in MCI frame
b	1	Onboard clock offset
d	1	Onboard clock drift

Some of the parameters used in the simulations are reported in Table 2 and most of them have been taken from previous work in Reference [9] for ease of performance comparison.

Table 2 Simulation parameters

Symbol	Description [units]	Value
$\boldsymbol{r}^{MCI}(t_0)$	True initial spacecraft position in MCI frame [km]	$\begin{bmatrix}1837.4 & 0.0 & 0.0\end{bmatrix}^T$
$\boldsymbol{v}^{MCI}(t_0)$	True initial spacecraft velocity in MCI frame [km/s]	$\begin{bmatrix}0.0 & 1.6335 & 0.0\end{bmatrix}^T$
$b(t_0)$	True initial onboard clock offset [s]	0.1
$d(t_0)$	True initial onboard clock drift [ND]	1e-4
$x_p,\ y_p$	Principal point [pixels]	$\begin{bmatrix}454.5 & 454.5\end{bmatrix}$
f	Camera focal length [pixels]	909
σ_α	Noise standard deviation on bearing angle α [pixels]	4.3921
σ_β	Noise standard deviation on bearing angle β [pixels]	4.3921
$\sigma_{\alpha\beta}$	Noise correlation between bearing angles α and β	0.0
σ_ρ	DSN range noise standard deviation [m]	43.4
$\sigma_{\dot{\rho}}$	DSN range rate noise standard deviation [m/s]	1
$\boldsymbol{Q}_{acc}$	Acceleration noise variance [m^2/s^4]	$(1e-6)^2\ \boldsymbol{I}_{3\times3}$
$h_0,\ h_{-1},\ h_{-2}$	Clock stability parameters [s, ND, s^{-1}]	$\begin{bmatrix}2e-19 & e-21 & 2e-20\end{bmatrix}$

A. Neglecting orbit-clock correlation

Figure 1.a-d shows the estimation errors (red lines) with the 3σ error bounds (blue lines) over a 12 hours simulation, and the innovation residuals are shown in Figure 1.e.

In this simulation the filter propagates the orbit states as if it was no clock error, but still estimates the clock states with the same two-states linear model defined before. No ground-based measurements are sent to the spacecraft in this scenario, that is, only craters optical navigation is performed.

It is important noticing that the values for the clock bias and drift used in these simulations are those of the low-end oscillator from Ref. [28]. This compensated crystal is not meant to keep un-aided spacecraft time, bur rather to be used in GPS receivers processing at least four pseudorange measurements consistently. While most spacecraft will probably select a more accurate onboard clock, the point to be taken is that in subsequent sections we are able to accurately keep an onboard time with this inexpensive oscillator nor without GPS nor DSN tracking. Additionally, the chosen clock values show the effectiveness of the proposed method within one-day simulations. More accurate clocks without ground steering would have the same trends, albeit after longer propagation times.

The position and velocity errors start diverging from the 3σ uncertainty bounds after about two hours because the filter is not taking into account that the measurements' timestamps are affected by the clock offset, whose estimation error also increases with time. The position and velocity errors are computed as the difference between the estimated state and the true state both evaluated at time t_k.

$$\delta \boldsymbol{x}_k = \boldsymbol{x}_k - \hat{\boldsymbol{x}}_k = \boldsymbol{x}(t_k) - \hat{\boldsymbol{x}}(t_k) \tag{58}$$

Let $\hat{t}_\ell$ be the estimated time whose numerical value coincides with the true time t_k, i.e. $\hat{t}_\ell = t_k$. Clearly $t_\ell = t_k$ only when the clock bias is zero. Filter divergence would slow down comparing the estimated state at t_ℓ with the true states at t_k. This asynchronous definition of localization error is not useful for an autonomous system that aims at making onboard decisions and it is therefore most concerned with the difference between the current true state and the current estimated state. If the onboard navigation state was downloaded to the ground to make decisions, on the other hand, the asynchronous error definition $\boldsymbol{x}(t_k) - \hat{\boldsymbol{x}}(t_\ell)$ would be appropriate because the ground would upload a command together with an execution time tag and a clock correction term. Hence remotely operated deep-space spacecraft typically do not necessitate the proposed time correlation terms.

Figure 1.e. shows the measurement residuals. Clearly, the filter propagates the spacecraft dynamics between each measurement and the following one for an incorrect amount of time: the error on clock drift estimate causes the clock offset estimation error to grow in the order of seconds after two hours. This causes the measurement update to fail, hence the innovations of the α angle start diverging.

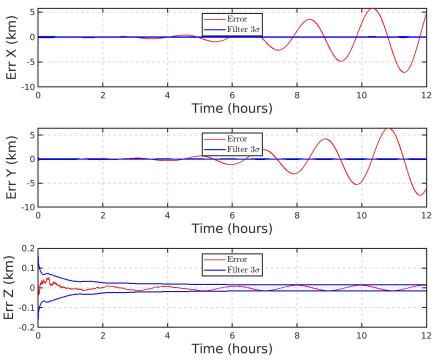

(a) Position estimation error.

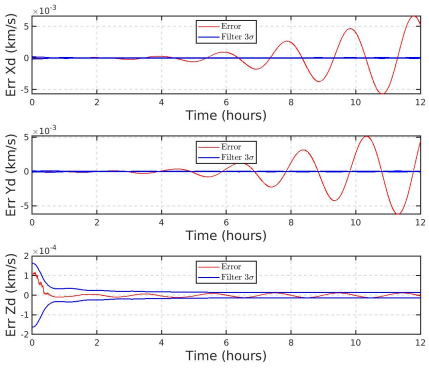

(b) Velocity estimation error.

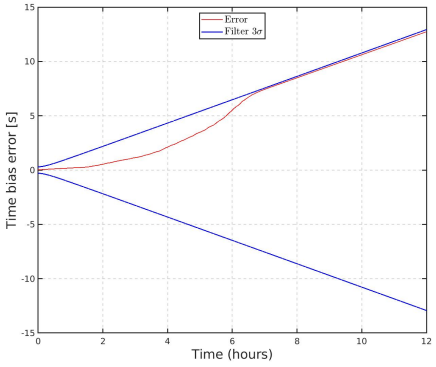

(c) Clock bias estimation error.

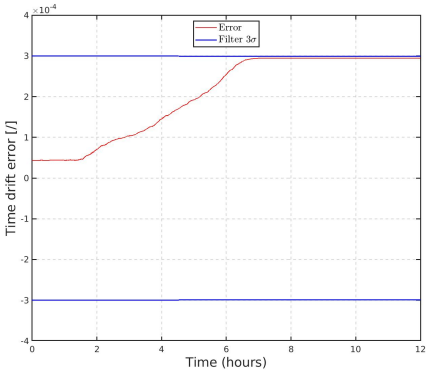

(d) Clock drift estimation error.

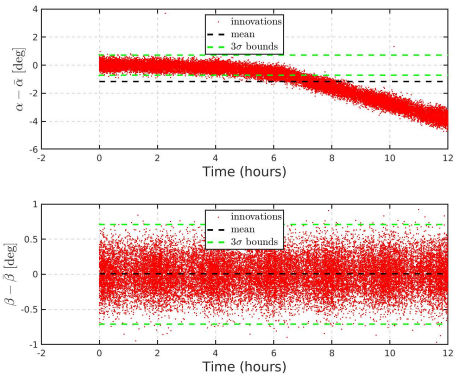

(e) Innovation residuals.

Fig. 1 Simulation results without accounting for clock offset.

B. Including orbit-clock correlation (Craters only)

Figure 2 shows 100 Monte Carlo runs when the new terms in the covariance propagation are included, and again processing craters measurements only. The duration of the simulation is one day.

We note that even using only optical measurements time-tagged with the onboard clock, the filter is able to estimate the clock drift. This is due to the clock error terms included in the covariance propagation and in the crater measurement

update equations. The filter is able to quickly reduce the error on clock drift (bottom right subfigure), preventing the error on clock offset to diverge too rapidly, as opposed to the previously shown scenario.

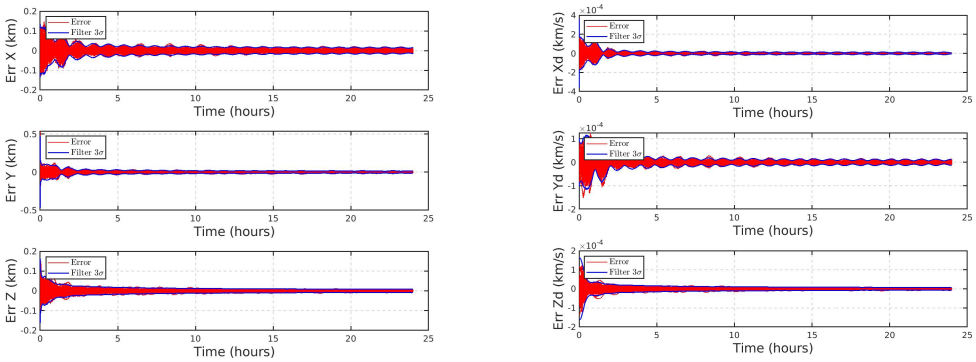

(a) Position estimation error.

(b) Velocity estimation error.

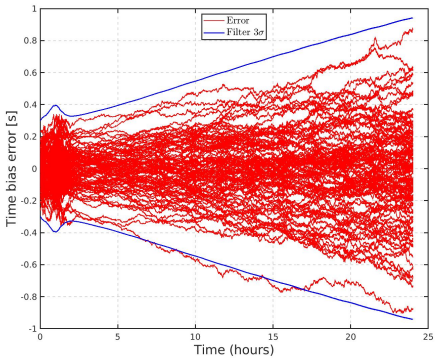

(c) Clock bias estimation error.

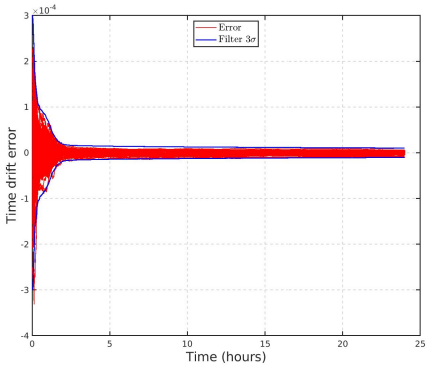

(d) Clock drift estimation error.

Fig. 2 Estimation errors with craters measurements only.

C. Including clock offset correlation (Craters and one-way ranging)

In this scenario, the filter processes craters measurements and one-way range measurements from DSN, using either all three stations (Figure 3), or only one station throughout the whole simulation (Figures 4, 5 and - 6 for Goldstone, Madrid and Canberra stations, respectively). Results show convergence of all state components with the uncertainty/error in the clock offset growing only with long periods without range measurements. Even in those phases the error on the onboard clock drift remains low so the error on clock bias does not grow too fast.

Most importantly, as it can be seen for example in the Goldston-only case (Figure 4), during the 15 hours tracking data gap there is no aliasing of the clock error into the position and velocity errors. This is again achieved through the added terms in the propagation equations that successfully deal with the correlation between the clock and the orbit states errors (without those terms, as it was shown in Figure 1, the orbit states errors would diverge in just a few hours).

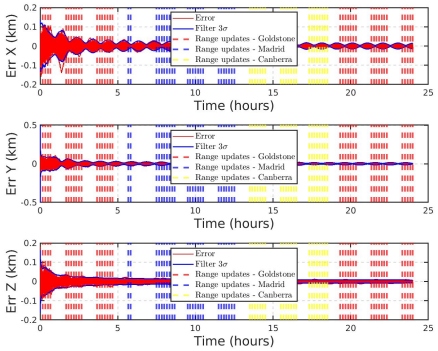

(a) Position estimation error.

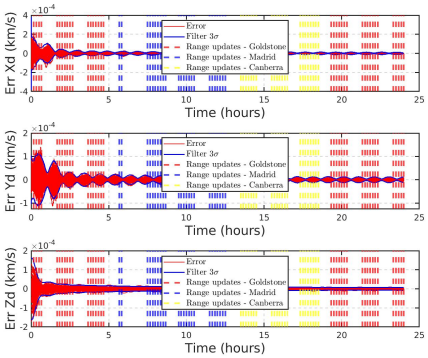

(b) Velocity estimation error.

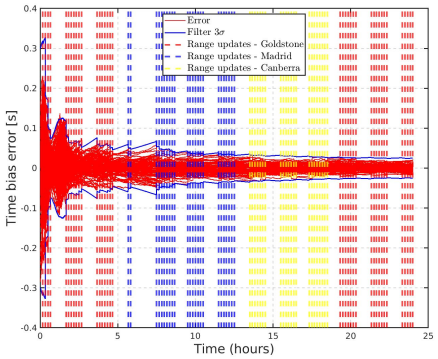

(c) Clock bias estimation error.

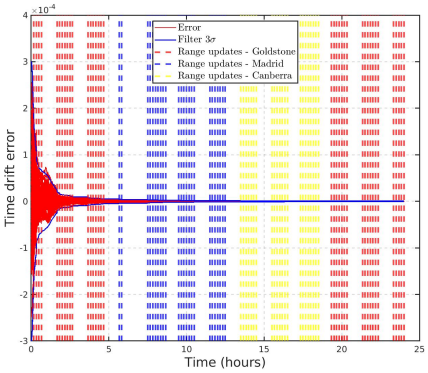

(d) Clock drift estimation error.

Fig. 3 Estimation errors with one-way ranging measurements.

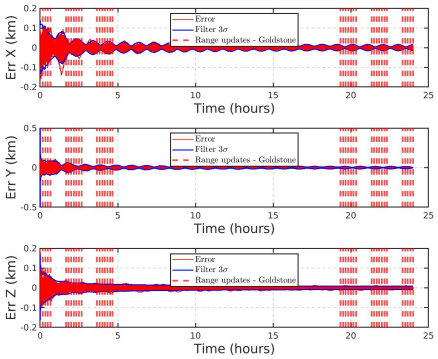

(a) Position estimation error.

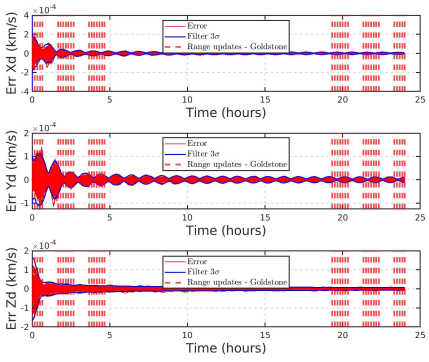

(b) Velocity estimation error.

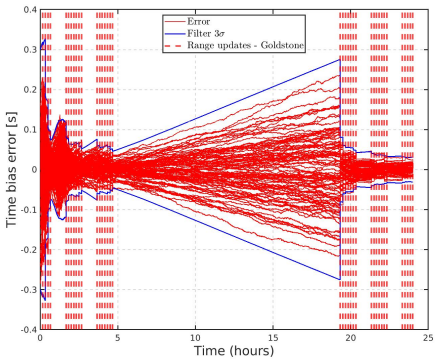

(c) Clock bias estimation error.

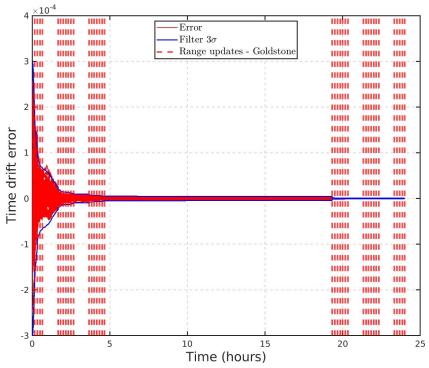

(d) Clock drift estimation error.

Fig. 4 Estimation errors with one-way ranging measurements from Goldstone station only.

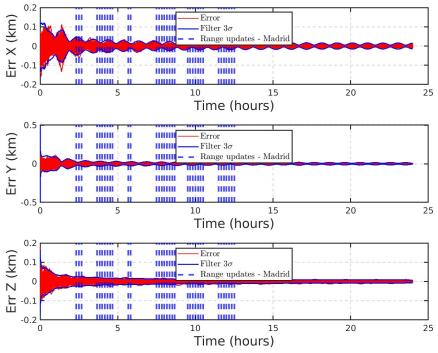

(a) Position estimation error.

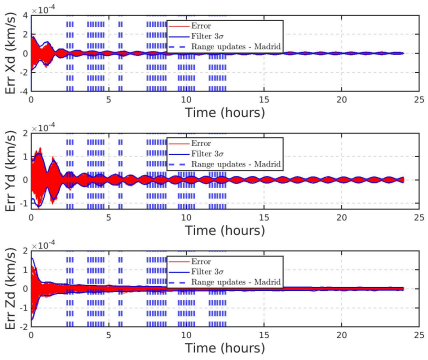

(b) Velocity estimation error.

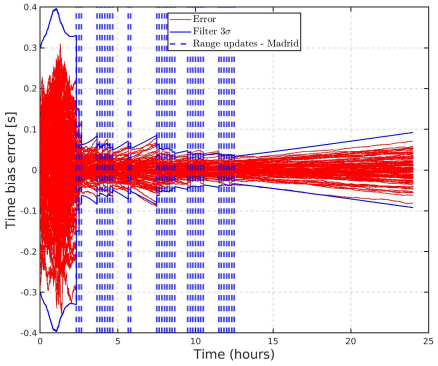

(c) Clock bias estimation error.

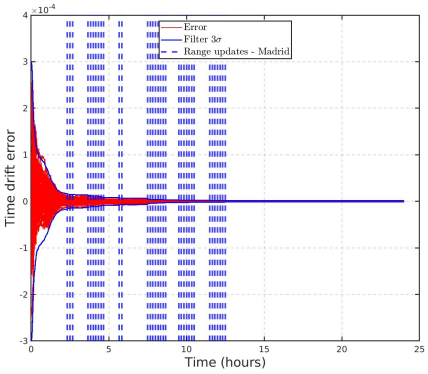

(d) Clock drift estimation error.

Fig. 5 Estimation errors with one-way ranging measurements from Madrid station only.

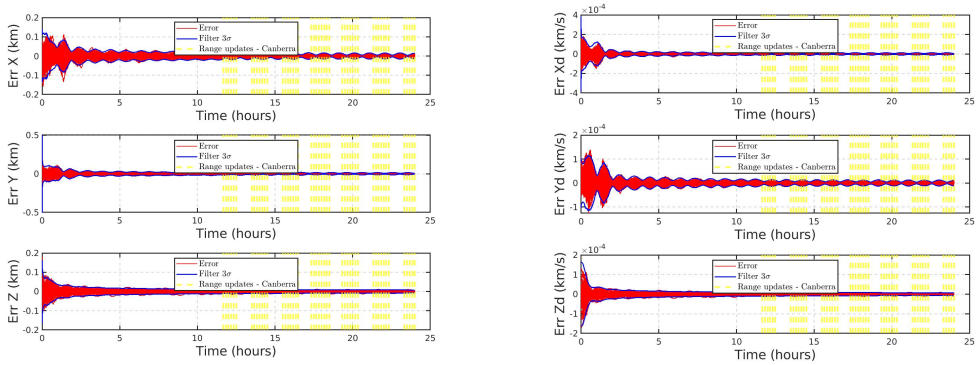

(a) Position estimation error.

(b) Velocity estimation error.

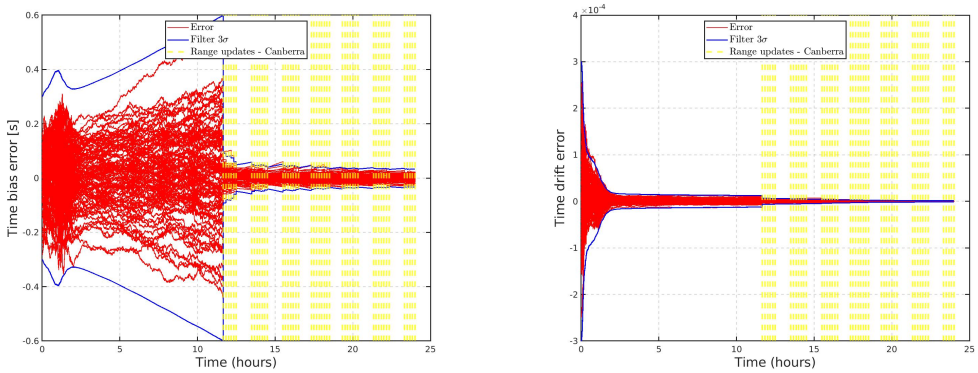

(c) Clock bias estimation error.

(d) Clock drift estimation error.

Fig. 6 Estimation errors with one-way ranging measurements from Canberra station only.

D. Including clock offset correlation (Craters and ground position updates)

Our formulation allows for onboard clock estimation from an externally provided measurement accurately time-tagged with an external reference clock. As a motivating example, we employ two-way tracking from DSN, for example in conjunction with spacecraft data downloads.

Figure 7 shows a Monte Carlo simulation with a position ground update performed every two hours. Results show the filter performance is similar to the one-way ranging case shown in the previous section.

Table 3 shows the root mean square errors of position components and clock states for one Monte Carlo trial from each simulation case.

The performance of the one-way ranging and the two-way position update are very close to each other.

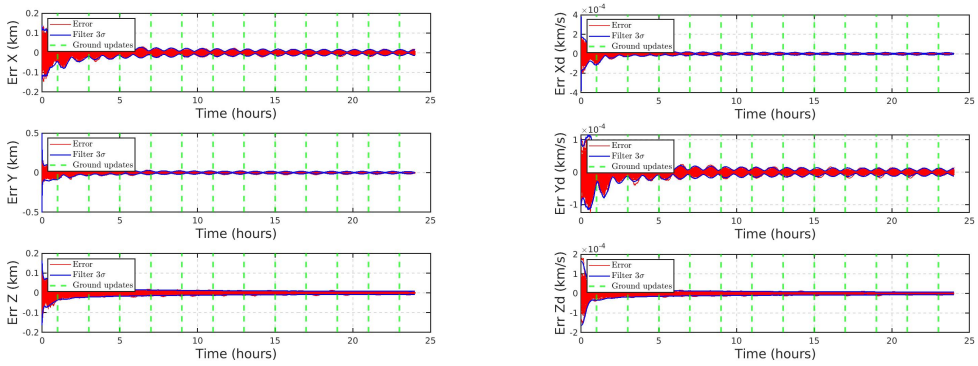

(a) Position estimation error. **(b) Velocity estimation error.**

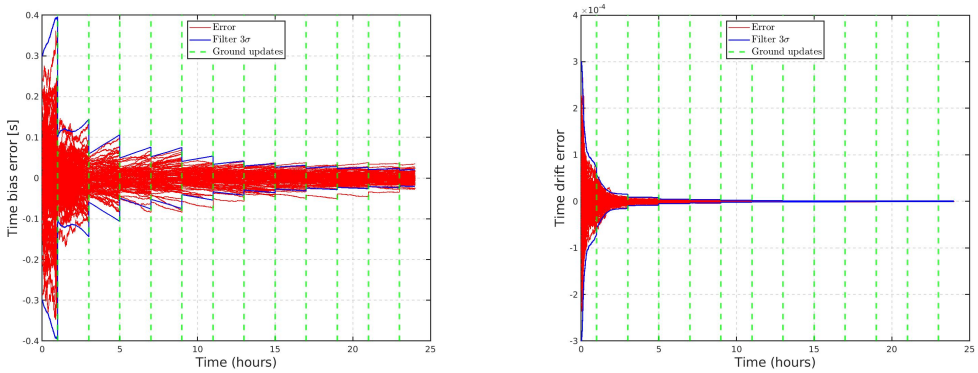

(c) Clock bias estimation error. **(d) Clock drift estimation error.**

Fig. 7 Estimation errors with craters measurements and position ground updates.

Table 3 RMS errors of one Monte Carlo trial for each simulation case

Case	RMS_x [km]	RMS_y [km]	RMS_z [km]	RMS_b [s]	RMS_d [/]
Neglecting orbit-clock correlation	2.322	2.478	0.01	7.05	2.27e-4
Including orbit-clock correlation(Craters only)	0.011	0.012	0.004	0.26	1.04e-5
Including orbit-clock correlation(Craters + all three DSN stations)	0.008	0.01	0.009	0.024	9.09e-6
Including orbit-clock correlation(Craters + Goldstone station only)	0.008	0.01	0.009	0.024	9.07e-6
Including orbit-clock correlation(Craters + Madrid station only)	0.008	0.01	0.009	0.048	1.00e-5
Including orbit-clock correlation(Craters + Canberra station only)	0.008	0.01	0.009	0.078	9.95e-6
Including orbit-clock correlation(Craters + position from ground)	0.01	0.015	0.005	0.039	1.28e-5

V. Conclusions

This work proposes a new approach to onboard position, navigation and timing in lunar orbit. Localization is performed via Moon crater relative navigation but no GPS measurements nor external clock corrections are available to the spacecraft. A novel formulation to deal with discrepancies between the onboard time and true time is developed.

The solution proposed consists of exploiting an extended Kalman filter algorithm accounting for correlation terms between timing errors and orbit states errors during the time propagation portion of the filter.

Numerical results show that the inclusion of these terms ensure convergence in the estimation errors of all filter states components in the scenario of Moon optical navigation without external time measurements and in two different configurations. The first one leverages one-way ranging from DSN to aid the onboard optical navigation, and the second one consists of a two-ways position update from DSN (without direct computation of onboard clock errors by the ground).

In particular, it is shown how the new formulation of the orbit and clock states time propagation prevents the localization error to diverge even with long gaps in tracking data. When DSN measurements are available, the filter is able to successfully reduce clock states estimation errors as well. With the standard two-states clock model adopted here, the clock drift error is reduced even in the optical-only simulated scenario, the addition of DSN measurements results in clock bias errors reduced as well.

Acknowledgments

Work completed at The University of Texas at Austin was conducted under NASA cooperative agreement 80NSSC20M0087.

References

[1] Turan, E., Speretta, S., and Gill, E., "Autonomous navigation for deep space small satellites: Scientific and technological advances," *Acta Astronautica*, Vol. 193, 2022, pp. 56–74. https://doi.org/10.1016/j.actaastro.2021.12.030.

[2] Ely, T., Bhaskaran, S., Bradley, N., Lazio, J. W., and Martin-Mur, T., "Comparison of Deep Space Navigation Using Optical Imaging, Pulsar Time-of-Arrival Tracking, and/ or Radiometric Tracking," *Journal of Astronautical Sciences*, Vol. 69, 2022, p. 385–472. https://doi.org//10.1007/s40295-021-00290-z.

[3] Bhaskaran, S., Riedel, J., Synnott, S., and Wang, T., "The Deep Space 1 autonomous navigation system - A post-flight analysis," *AIAA-2000-3935, Astrodynamics Specialist Conference, Denver, CO*, 2000. https://doi.org/10.2514/6.2000-3935.

[4] Kubitschek, D. G., Mastrodemos, N., Werner, R. A., Kennedy, B. M., Synnott, S. P., Null, G. W., Bhaskaran, S., Riedel, J. E., and Vaughan, A. T., "Deep Impact Autonomous Navigation : the trials of targeting the unknown," *AAS 06-081, AAS Guidance and Control Conference, Breckenridge, CO*, 2006.

[5] Bhaskaran, S., "Autonomous Navigation for Deep Space Missions," *12th International Conference on Space Operations, Stockholm, Sweden*, 2012. https://doi.org/10.2514/6.2012-1267135.

[6] Hur-Diaz, S., Bamford, B., and Gaylor, D., "Autonomous lunar orbit navigation using optical sensors," *Astrodynamics 2007*

- *Advances in the Astronautical Sciences, Proceedings of the AAS/AIAA Astrodynamics Specialist Conference*, 2008, pp. 997–1014.

[7] Hinga, M. B., and Williams, D., "Autonomous Cis-Lunar Navigation using Optical Measurements to a Lunar Landmark," *Proceedings of the 2022 International Technical Meeting of The Institute of Navigation, Long Beach, California*, 2022, pp. 485–495. https://doi.org/10.33012/2022.18192.

[8] Kaplev, S., Titov, M., Valentirova, T., Mozharov, I., Bolkunov, A., and Yaremchuk, V., "Lunar PNT system concept and simulation results," *Open Astronomy*, Vol. 31, No. 1, 2022, pp. 110–117. https://doi.org/doi:10.1515/astro-2022-0014, URL https://doi.org/10.1515/astro-2022-0014.

[9] McLaughlin, Z. R., Gold, R. E., Catalan, S. G., Moghe, R., Jones, B. A., and Zanetti, R., "Crater navigation and timing for autonomous lunar orbital operations in small satellites," *AAS 22-146, AAS Guidance, Navigation, and Control Conference, Breckenridge, CO*, 2022.

[10] Christian, J. A., "Optical Navigation Using Planet's Centroid and Apparent Diameter in Image," *Journal of Guidance, Control, and Dynamics*, Vol. 38, No. 2, 2015, pp. 192–204. https://doi.org/10.2514/1.G000872.

[11] Franzese, V., Lizia, P. D., and Topputo, F., "Autonomous Optical Navigation for LUMIO Mission," *AIAA 2018-1977, 2018 Space Flight Mechanics Meeting*, 2018. https://doi.org/10.2514/6.2018-1977.

[12] Holt, G. N., D'Souza, C. N., and Saley, D. W., "Orion Optical Navigation Progress Toward Exploration Mission 1," *AIAA 2018-1978, 2018 Space Flight Mechanics Meeting*, 2018. https://doi.org/10.2514/6.2018-1978.

[13] Hill, K., Martin W, L., and Born, G., "Linked, Autonomous, Interplanetary Satellite Orbit Navigation (Li-AISON) in Lunar Halo Orbits," *AAS 05-399, AAS/AIAA Astrodynamics Specialist Conference, Lake Tahoe, CA*, 2005.

[14] Hesar, S. G., Parker, J. S., Leonard, J. M., McGranaghan, R. M., and Born, G. H., "Lunar far side surface navigation using Linked Autonomous Interplanetary Satellite Orbit Navigation (LiAISON)," *Acta Astronautica*, Vol. 117, 2015, pp. 116–129. https://doi.org/10.1016/j.actaastro.2015.07.027.

[15] Thompson, M., Forsman, A., Peters, B., Ely, T., Sorensen, D., and Cheetham, B., "Cislunar Navigation Technology Demonstrations on the CAPSTONE Mission," *Proceedings of the 2022 International Technical Meeting of The Institute of Navigation*, 2022, pp. 471–484. https://doi.org/10.33012/2022.18208.

[16] Mitchel, J., Winternitz, L., Hassouneh, M., Price, S., Semper, S., Yu, W., Ray, P., Wolff, M. T., Kerr, M., Wood, K. S., Arzoumanian, Z., Gendreau, K. C., Guillemot, L., Cognard, I., and Demorest, P., "SEXTANT X-ray Pulsar Navigation Demonstration: Initial On-Orbit Results," *AIAA 18-155, AAS Guidance and Control Conference, Breckenridge, CO*, 2018.

[17] Winternitz, L., Hassouneh, M., Mitchel, J., Price, S., Yu, W., Semper, S., Ray, P., Wood, K. S., Arzoumanian, Z., and Gendreau, K. C., "SEXTANT X-ray Pulsar Navigation Demonstration: Additional On-Orbit Results," *AIAA 2018-2538, 15th International Conference on Space Operations, Marseille, France*, 2018. https://doi.org/10.2514/6.2018-2538.

[18] Ely, T., and Seubert, J., "Advancing Navigation, Timing, and Science with the Deep Space Atomic Clock," *AIAA 2014-1856, 13th International Conference on Space Operations*, 2014. https://doi.org/10.2514/6.2014-1856.

[19] Oudrhiri, K., Yang, O., Buccino, D., Kahan, D., Withers, P., Tortora, P., Matousek, S., Lay, N., Lazio, J., Krajewski, J., and Klesh, A., "MarCO Radio Occultation: How the First Interplanetary Cubesat Can Help Improve Future Missions," *2020 IEEE Aerospace Conference, Big Sky, MT*, 2020, pp. 1–10. https://doi.org/10.1109/AERO47225.2020.9172734.

[20] Ely, T., Seubert, J., Bradley, N., Drain, T., and Bhaskaran, S., "Radiometric Autonomous Navigation Fused with Optical for Deep Space Exploration," *Journal of Astronautical Sciences*, Vol. 68, 2021, p. 300–325. https://doi.org//10.1007/s40295-020-00244-x.

[21] Seubert, J., Ely, T. A., and Stuart, J., "Results of the Deep Space Atomic Clock Deep Space Navigation Analog Experiment," *Journal of Spacecraft and Rockets*, Vol. 59, No. 6, 2022, pp. 1914–1925. https://doi.org/10.2514/1.A35334.

[22] Allan, D. W., Gray, J. E., and Machlan, H. E., "The National Bureau of Standards Atomic Time Scale: Generation, Stability,Accuracy and Accessibility," *NBS Monograph 140, Time and Frequency: Theory and Fundamentals, National Institute of Standards and Technology*, 1974, p. 205–231. https://doi.org/10.1109/TIM.1972.4314051.

[23] Farrell, J., "Aided Navigation GPS with High Rate Sensors," McGraw-Hill, 2008, pp. 281–287.

[24] "IEEE Standard Definitions of Physical Quantities for Fundamental Frequency and Time Metrology-Random Instabilities," *IEEE Std 1139-1999*, 1999, pp. 1–40. https://doi.org/10.1109/IEEESTD.1999.90575.

[25] Tryon, P. V., and Jones, R. H., "Estimation of parameters in models for cesium beam atomic clocks," *J. Res. National Bureau of Standards*, Vol. 88, No. 1, 1983. https://doi.org/10.6028/jres.088.001.

[26] Stein, S. R., and Filler, R. L., "Kalman Filter Analysis for Real Time Applications of Clocks and Oscillators," *42nd annual Frequency control symposium*, 1988, pp. 447–452. https://doi.org/10.1109/FREQ.1988.27638.

[27] Dierendonck, A. J. V., McGraw, J. B., and Brown, R. G., "Relationship between Allan variances and Kalman filter parameters," *Proceedings of the 16th Annual Precise Time and Time Interval (PTTI) Applications and Planning Meeting, NASA Goddard Space Flight Center*, 1984, pp. 273–293.

[28] Brown, R. G., and Hwang, P. Y. C., "Introduction to Random Signals and Applied Kalman Filtering, 3rd ed." John Wiley and Sons, 1996, pp. 428–432.

[29] Shmaliy, Y. S., and Ibarra-Manzano, O. G., "Clock Current State Estimation with a Kalman-Like Algorithm Employing Measurement of Time Errors," *2011 Joint Conference of the IEEE International Frequency Control Symposium and European Frequency and Time Forum*, 2011, pp. 1–4. https://doi.org/10.1109/FCS.2011.5977274.

[30] Contreras-Gonzalez, J., Ibarra-Manzano, O., and Shmaliy, Y. S., "Clock state estimation with the Kalman-like UFIR algorithm via TIE measurement," Vol. 46, 2012, pp. 476–483. https://doi.org/10.1016/j.measurement.2012.08.003.

[31] Guanwen Huang, Q. Z., "Real-time estimation of satellite clock offset using adaptively robust Kalman filter with classified adaptive factors," Vol. 16, 2012, pp. 531–539. https://doi.org/10.1007/s10291-012-0254-z.

[32] Huang, B., Ji, Z., Zhai, R., Xiao, C., Yang, F., Yang, B., and Wang, Y., "Clock bias prediction algorithm for navigation satellites based on a supervised learning long short-term memory neural network," *GPS Solutions*, Vol. 25, 2021. https://doi.org/10.1007/s10291-021-01115-0.

[33] Holt, G. N., and Lightsey, E. G., "In Situ Navigation of Spacecraft Formations in High-Altitude and Extraterrestrial Orbits," *Journal of Spacecraft and Rockets*, Vol. 45, No. 2, 2008, pp. 299–308. https://doi.org/10.2514/1.29361.

[34] Tapley, B. D., Schutz, B. E., and Born, G. H., "Statistical Orbit Determination," Elsevier Academic Press, 2004, pp. 501–505. https://doi.org/10.1016/B978-0-12-683630-1.X5019-X.

[35] Speyerer, E., Robinson, M., Denevi, B., et al., "Lunar Reconnaissance Orbiter Camera global morphological map of the Moon," *42nd Annual Lunar and Planetary Science Conference*, 2011, p. 2387.

[36] Robbins, S. J., "A New Global Database of Lunar Impact Craters >1–2 km: 1. Crater Locations and Sizes, Comparisons With Published Databases, and Global Analysis," *Journal of Geophysical Research: Planets*, Vol. 124, No. 4, 2019, pp. 871–892. https://doi.org/10.1029/2018JE005592.

[37] Munkres, J., "Algorithms for the Assignment and Transportation Problems," *Journal of the Society for Industrial and Applied Mathematics*, Vol. 5, No. 1, 1957, pp. 32–38. https://doi.org/10.1137/0105003.

[38] Murty, K. G., "Letter to the Editor—An Algorithm for Ranking all the Assignments in Order of Increasing Cost," *Operations Research*, Vol. 16, No. 3, 1968, pp. 682–687. https://doi.org/10.1287/opre.16.3.682.